2017

The Effect of Comb Architecture on Complex Coacervation

Brandon M. Johnston
University of Massachusetts Amherst

Cameron W. Johnston
University of Massachusetts Amherst

Rachel A. Letteri
University of Massachusetts Amherst

Tyler K. Lytle
University of Illinois at Urbana-Champaign

Charles E. Sing
University of Illinois at Urbana-Champaign

See next page for additional authors

Recommended Citation

Johnston, Brandon M.; Johnston, Cameron W.; Letteri, Rachel A.; Lytle, Tyler K.; Sing, Charles E.; Emrick, Todd; and Perry, Sarah L., "The Effect of Comb Architecture on Complex Coacervation" (2017). *Organic & Biomolecular Chemistry*. 841.
https://doi.org/10.1039/C7OB01314K

The Effect of Comb Architecture on Complex Coacervation

Brandon M. Johnston,[a] Cameron W. Johnston,[a] Rachel A. Letteri,[b] Tyler K. Lytle,[c] Charles E. Sing,[e] Todd Emrick,[b] and Sarah L. Perry*[a]

Complex coacervation is a widely utilized technique for effecting phase separation, though predictive understanding of molecular-level details remains underdeveloped. Here, we couple coarse-grained Monte Carlo simulations with experimental efforts using a polypeptide-based model system to investigate how a comb-like architecture affects complex coacervation and coacervate stability. Specifically, the phase separation behavior of linear polycation-linear polyanion pairs was compared to that of comb polycation-linear polyanion and comb polycation-comb polyanion pairs. The comb architecture was found to mitigate cooperative interactions between oppositely charged polymers, as no discernible phase separation was observed for comb-comb pairs and complex coacervation of linear-linear pairs yielded stable coacervates at higher salt concentration than linear-comb pairs. This behavior was attributed to differences in counterion release by linear vs. comb polymers during polyeletrolyte complexation. Additionally, the comb polycation formed coacervates with both stereoregular poly(*L*-glutamate) and racemic poly(*D,L*-glutamate), whereas the linear polycation formed coacervates only with the racemic polyanion. In contrast, solid precipitates were obtained from mixtures of stereoregular poly(*L*-lysine) and poly(*L*-glutamate). Moreover, the formation of coacervates from cationic comb polymers incorporating up to ~90% pendant zwitterionic groups demonstrated the potential for inclusion of comonomers to modulate the hydrophilicity and/or other properties of a coacervate-forming polymer. These results provide the first detailed investigation into the role of polymer architecture on complex coacervation using a chemically and architecturally well-defined model system, and highlight the need for additional research on this topic.

1. Introduction

Complex coacervation is a liquid-liquid phase separation driven by the electrostatic interaction of oppositely charged polyelectrolytes in water that results in a dense, polymer-rich coacervate phase in equilibrium with a polymer-poor supernatant phase (Figure 1).[1-5] These coacervates are initially present as droplets in solution, and can be coalesced by sedimentation or centrifugation. While coacervate-based materials have a long history in the food and personal care industries,[6-11] and more recent application in drug delivery and biomedical adhesives,[12-14] a detailed and predictive understanding of how molecular-level details impact the formation and properties of this class of materials remains underdeveloped.[4]

Coacervation occurs by electrostatic attraction between oppositely charged macromolecules and the entropically favourable release of counterions and restructuring of water molecules.[15-19] As a result, parameters such as the polymer charge stoichiometry, linear charge density along the polymer chain, pH, ionic strength, and polymer concentration effectively modulate the self-assembly and responsiveness of these materials.[20-24] The development of a detailed and predictive understanding of the molecular-level effects of polymer chemistry and architecture has historically been limited due to the poorly defined chemical and physical properties of many of the naturally derived polymers that have dominated this literature.[3,5,7,25-28] However, recent advances in polymer chemistry have enabled the controlled synthesis of a diverse palette of polymers with precisely defined chemical and physical properties.[29-34] For instance, synthetic polypeptides have been used extensively as model systems to examine the effects of different side chain moieties pendant to a polypeptide backbone through incorporation of various amino acids.[29,35-47] Furthermore, solid-phase synthesis enables precise control over the sequence and presentation of chemical functionality.[48-50]

To date, most studies of complex coacervation have focused on the impact of specific chemistries, with relatively few reports investigating the effect of polymer architecture. Here, we utilize polypeptide-based comb polymers to investigate the effects of branching on the self-assembly and

[a] *Department of Chemical Engineering, University of Massachusetts Amherst, Amherst, MA 01003, USA.*
[b] *Department of Polymer Science & Engineering, University of Massachusetts Amherst, Amherst, MA 01003, USA*
[c] *Department of Chemistry, University of Illinois at Urbana-Champaign, Urbana, IL 61801*
[d] *Department of Chemical & Biomolecular Engineering, University of Illinois at Urbana-Champaign, Urbana, IL 61801.*
* Correspondence Email: perrys@engin.umass.edu
Electronic Supplementary Information (ESI) available: Polymerization data. Monomer:catalyst ratios used to synthesize *L*K5SB-X. ^{1}H-NMR spectra of *L*E5-COE, *L*K5SB-44, *L*K5, and *L*E5. SEC-MALS trace of *L*E5. Turbidity data testing the order of polymer addition. See DOI: 10.1039/x0xx00000x

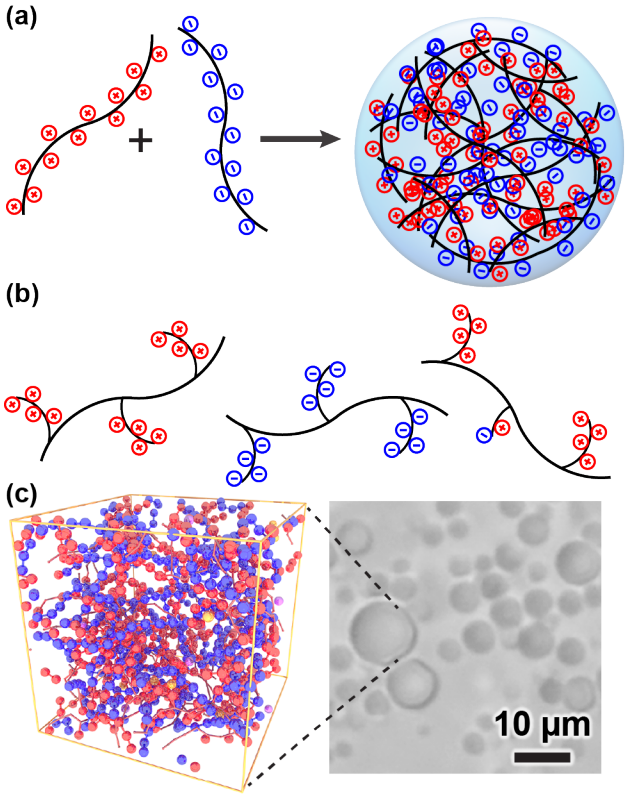

Figure 1. (a) Schematic depiction of complex coacervation between two oppositely charged linear polymers. **(b)** Comb polymer architectures, including cationic (red) and anionic (blue) comb polymers, and a copolymer of cationic and zwitterionic moieties. **(c)** Coacervation is observed as droplets of a polymer-dense coacervate dispersed in a polymer-dilute supernatant phase. Monte Carlo simulations are used to provide a coarse-grained representation of coacervation, taking molecular architecture into account. The optical micrograph shows a coacervate phase formed from a comb polycation (red) and linear polyanion (blue).

stability of complex coacervates. Furthermore, we investigate the effect of hydrophilic zwitterionic moieties (*i.e.*, net-neutral groups with both positive and negative charges on the same monomer unit) as comonomers within comb polymers without altering the local charge density of the polymer (Figure 1b).[51-56] Zwitterions are of particular interest in the context of complex coacervation since they increase polymer solubility, and open opportunities for electrostatic interactions between the dipole of the zwitterion and the charge on the polymer.[57-59] Our studies showed that while architecture did not significantly impact the charge stoichiometries yielding complex coacervates, the comb architecture markedly decreased the salt stability relative to equivalent linear coacervates. Additionally, the incorporation of zwitterionic moieties, up to *ca*. 90 mol% within cationic comb polymers, did not disrupt coacervate formation, suggesting the potential for incorporation of high loadings of zwitterions or other comonomers into these structures.

2. Experimental Section

2.1. Materials

Dichloromethane (DCM, ≥99.5%) and dimethylformamide (DMF, ≥99.5%) were purchased from Fisher Bioreagents. *N*,*N*-diisopropylethyleamine (DiPEA, ≥99%), 1-[bis(dimethylamino)methylene]-1*H*-1,2,3-triazolo[4,5-*b*]pyridinium 3-oxid hexaflurophosphate (HATU, 97%), hydrogen chloride solution (4M in dioxane), ethyl vinyl ether (99%), methanol (anhydrous MeOH, 99.8%), triisopropylsilane (TiPS, 99%), and Ramage ChemMatrix Resin (0.3-0.6 mmol/g, 35-100 mesh) were purchased from Sigma-Aldrich. Trifluoroacetic acid (TFA, ≥99%), 1-hydroxybenztriazole monohydrate (HOBt hydrate, ≥98%), and Fmoc-Lys(Boc)-preloaded 2-chlorotrityl chloride resin (0.3-1.5 mmol/g, 100-200 mesh) were purchased from Advanced ChemTech. 2,2,2-Trifluoroethanol (TFE, ≥99%) was purchased from Alfa Aesar. Sodium chloride (NaCl) and sodium bicarbonate were purchased from Fisher Chemical. Fmoc-Lys(Boc)-OH and Fmoc-Glu(OtBu)-OH were purchased from Peptide Solutions, LLC. Diethyl ether (stabilized by butylated hydroxytoluene (BHT)) and dialysis tubing (molecular weight cut-off, MWCO = 6-8 kDa) were purchased from Fisher Scientific. Piperidine (≥99%) was purchased from EMD Millipore Corporation. Poly(*D,L*-glutamate sodium salt) (avg. MW=15000 g/mol), poly(*L*-glutamate sodium salt) (avg. MW=15000 g/mol), poly(*D,L*-lysine hydrobromide) (avg. MW=21000 g/mol), and poly(*L*-lysine hydrobromide) (avg. MW=21000 g/mol) were purchased from Alamanda Polymers, Inc. Water was dispensed from a Milli-Q purification system at a resistivity of 18.2 MΩ-cm. (*Z*)-Cyclooct-4-ene-1-carboxylic acid (COE-COOH) was synthesized from 1,5-cyclooctadiene as previously reported.[60-62] 3-Bromopyridine-substituted Grubbs Generation III catalyst (G3-BrPy) was synthesized according to a literature procedure.[63] Sulfobetaine-substituted cyclooctene (SB-COE) was synthesized from dimethylaminoethyl cyclooctene according to the literature.[64] All other chemicals were used without further purification or modification.

2.2. Characterization

^{1}H NMR spectra of Boc- and *t*Bu-protected oligopeptide-substituted cyclooctene monomers and deprotected charged polymers were recorded on either a Bruker Spectrospin DPX300 or a Bruker Ascend 500 spectrometer equipped with a Prodigy cryoprobe. Mass spectrometry was performed on a Bruker MicroFlex LRF matrix-assisted laser desorption/ionization time of flight mass spectrometer (MALDI-TOF). Size exclusion chromatography (SEC) on deprotected cationic pentalysine comb polymers was performed in TFE with 0.02 M sodium trifluoroacetate at 40°C using an Agilent 1200 system equipped with an isocratic pump operated at 1 mL/min, a degasser, an autosampler, one 50 x 8 mm PSS PFG guard column (Polymer Standards Service), three 300 x 7.5 mm PSS PFG analytical linear M columns with a 7 µm particle size (Polymer Standards Service), and an Agilent 1200 refractive index detector. The system was calibrated with linear PMMA standards. SEC equipped with a multi-angle light scattering detector (SEC-MALS) was performed on the deprotected pentaglutamate comb polymer in aqueous

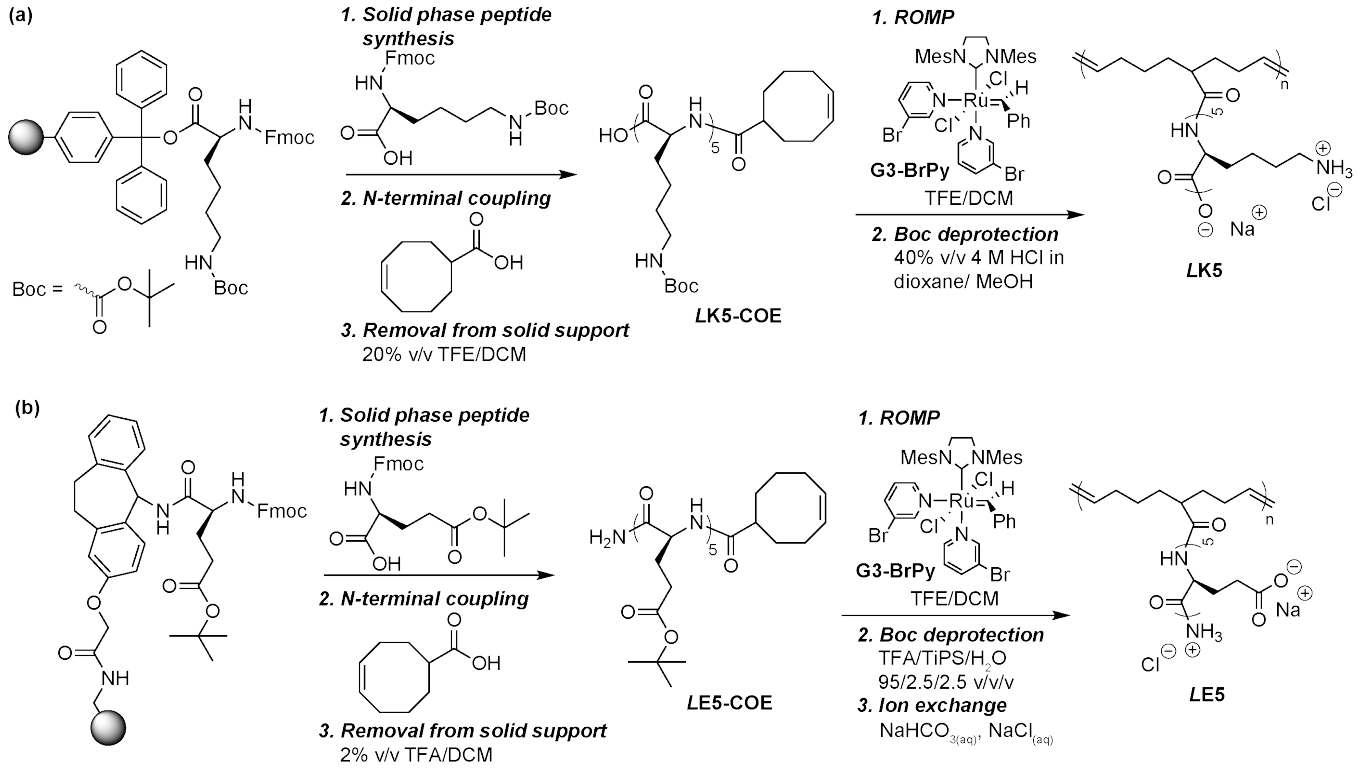

Figure 2. (a) Synthesis and polymerization of oligolysine-substituted cyclooctenes. Lysine-based oligopeptides were prepared *via* solid-phase peptide synthesis utilizing a 2-chlorotrityl chloride resin preloaded with Fmoc-protected lysine. Following repeated addition of Fmoc-protected lysine and removal of the Fmoc group with a 20% piperidine/DMF solution, cyclooct-4-ene-1-carboxylic acid was coupled to the *N*-terminus. The resin was cleaved from the peptide following synthesis using a 20% v/v TFE /DCM solution, exposing the *C*-terminal carboxylic acid to give ***L*K5-COE**. ROMP using the G3-BrPy catalyst, followed by Boc removal in highly acidic conditions yielded the positively charged lysine comb polymer ***L*K5**. **(b)** Synthesis and polymerization of pentaglutamic acid-substituted cyclooctene. Glutamate-based peptides were prepared *via* solid-phase peptide synthesis utilizing a glutamate-preloaded Ramage ChemMatrix resin and capped with cyclooct-4-ene-1-carboxylic acid. The resin was cleaved from the peptide following synthesis using a 2% v/v TFA/DCM solution, exposing a *C*-terminal amide and yielding ***L*E5-COE**. **(b)** ROMP using the G3-BrPy catalyst, followed by acid-catalyzed cleavage of the *t*-Bu groups to yield the negatively charged oligoglutamate-substituted comb polymer ***L*E5**.

solution with 5% ammonium phosphate and 3% acetonitrile at 25°C. SEC-MALS was operated with a flow rate of 0.5 mL/min on a Wyatt system equipped with a TSKgel G2000SWxl column (15 cm, 5 µm particle size, Tosoh Bioscience, LLC), a DAWN HELEOS II MALS detector (664 nm), and an Optilab T-rEX refractive index detector.

2.3. Synthesis of 5-[K(Boc)]$_5$-1-cyclooctene (*L*K5-COE) and 5-[E(OtBu)]$_5$-1-cyclooctene (*L*E5-COE)

Penta-L-lysine-substituted cyclooctene (*L*K5-COE) was synthesized either by hand following previously published procedures,[48,65] or by automated peptide synthesis as described here for penta-L-glutamate-substituted cyclooctene (*L*E5-COE). Solid-phase peptide synthesis[49] was used to prepare *L*E5-COE utilizing a CEM Liberty Blue peptide synthesizer equipped with a CEM Discover attachable microwave and HT12 high-throughput attachment. Fmoc-Glu(*t*-Bu)-preloaded Ramage resin (0.494 g, 0.51 mmol/g, 35-100 mesh) was swollen in a DCM/DMF mixture (50% v/v), followed by deprotection of the Fmoc group using a piperidine/DMF solution (25% v/v) to yield a free amine. Addition of Fmoc-Glu(*t*-Bu)-OH (0.2 M in DMF) and subsequent Fmoc removal was repeated 4x to produce penta-L-glutamate oligopeptide chains. Amino acid coupling was assisted by HATU (0.5 M in DMF) and DiPEA (2 M in DMF). (*Z*)-Cyclooct-4-ene-1-carboxylic acid (0.2 M in DMF) was then coupled to the *N*-terminus of the peptide, and the cyclooctene-modified, resin-attached peptide was transferred to a 50 mL peptide vessel, washed with DCM (~25 mL), and cleaved from the resin with a TFE solution (20% v/v in DCM). The resulting solution was concentrated under reduced pressure to ~2 mL and precipitated into diethyl ether (40 mL). The precipitate was isolated by centrifugation (4000 rpm, 5 min) and dried under vacuum to afford *L*E5-COE as a flaky white solid in 38% yield (0.23 g). MALDI-TOF mass spectrometry: calculated $[M + Na]^+$ 1101.63, found 1101.90. ^{1}H NMR (500 MHz, DMSO-d_6, δ, ppm): 7.72-8.18 (br m, 5H), 6.98-7.72 (br m, 2H), 5.53-5.81 (br m, 2H), 4.04-4.51 (br m, 5H), 1.30-2.44 (br m, 76H).

2.4. Representative Polymerization of Oligopeptide- and SB-substituted Cyclooctenes

Polymerizations and subsequent removal of peptide protecting groups were conducted similarly as previously reported.[64] *L*K5-COE (0.20 g, 0.15 mmol) and SB-COE (0.080 g, 0.23 mmol) were dissolved in TFE (0.71 mL) in a scintillation vial equipped with a stir bar and a septum. The monomer solution was subjected to three freeze–pump–thaw cycles. Separately, a solution of 3-bromopyridine-substituted Grubbs'

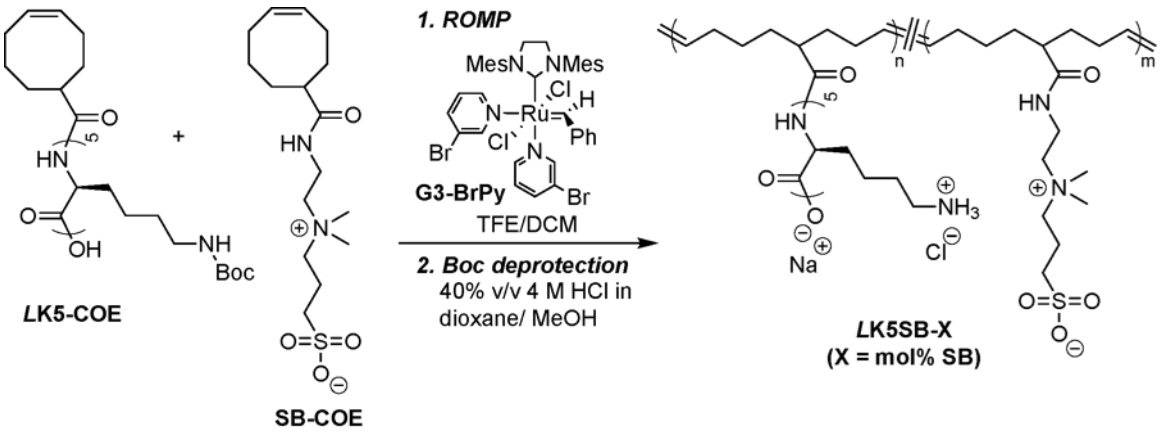

Figure 3. Synthesis of zwitterion-containing comb polymers by ROMP of oligolysine- and sulfobetaine- (SB) substituted cyclooctenes, holding the [*L*K5-COE]:[G3-BrPy catalyst] molar ratio constant and varying the SB-COE feed ratio. Subsequent removal of Boc groups yielded a series of positively charged, zwitterion-containing oligolysine comb polymers, named *L*K5SB-X, where X = mol% SB compared to total monomer (pentalysine and SB).

metathesis catalyst (G3-BrPy) was prepared in DCM (50 mg/mL) and subjected to three freeze–pump–thaw cycles. The catalyst solution (0.003 g, 0.004 mmol, 0.06 mL) was added to the monomer and the mixture was stirred for 2 h at room temperature under $N_{2(g)}$. Ethyl vinyl ether (0.10 mL, 0.075 g, 1.0 mmol) was added, and the mixture was stirred 30 min and opened to ambient atmosphere. The mixture was diluted with TFE (1 mL) and precipitated into diethyl ether (40 mL). The precipitate was isolated by centrifugation (4000 rpm, 5 min) and dried under vacuum to afford a mixture of monomer and polymer as a yellow-brown solid (86% mass recovery). The precipitate (0.24 g) was dissolved in MeOH (~12 mL) and 4 M HCl in dioxane (~5 mL). The mixture was stirred for 3 h at room temperature while open to atmosphere, then precipitated into diethyl ether (~160 mL). The precipitate was isolated by centrifugation (4000 rpm, 5 min) then dissolved in water and adjusted to pH 7-8 with sodium bicarbonate. The solution was dialyzed in water (6–8 kDa MWCO membrane) and lyophilized to afford a white powder (20-50% yield), where the theoretical yield was calculated as (mass of the Boc-protected polymer and monomer mixture used in the deprotection reaction, g)*(monomer conversion)*(average molecular weight per repeat unit deprotected polymer with counterions, g/mol)/(average molecular weight per repeat unit Boc-protected polymer, g/mol). ^{1}H NMR (300 MHz, D_2O, δ): 5.35 (br, 2H from *L*K5 and 2H from SB), 3.98-4.47 (br m, 5H from *L*K5), 3.29-3.86 (br m, 6H from SB), 3.14 (br, 6H from SB), 2.67-3.03 (br, 10H from *L*K5 and 2H from SB), 2.09-2.49 (br, 1H from *L*K5 and 3H from SB), 1.05-2.09 (br m, 40 H from *L*K5 and 10H from SB). Molecular weights estimated relative to PMMA standards by SEC eluting in TFE with 0.02 M sodium trifluoroacetate relative and compositions determined by ^{1}H NMR spectroscopy are provided in Table 1, and the monomer:catalyst feed ratios for all copolymerizations are provided in Table S1. Percent SB incorporation was calculated by ^{1}H NMR spectroscopy, comparing the relative intensities of the SB quarternary ammonium resonances at 3.1 ppm to the lysine δ and SB methylene protons adjacent to the sulfonate between 2.8-3.0 ppm.

Poly(K5-COE), LK5: Monomer solution: *L*K5-COE (0.20 g, 0.15 mmol) in TFE (0.2 mL); catalyst (0.003 g, 0.003 mmol, 0.05 mL). Deprotection solution: precipitate (0.1 g) in MeOH (anhydrous, ~5 mL) and 4 M HCl in dioxane (~2 mL). Yield: 60% (29 mg). ^{1}H NMR (300 MHz, D_2O, δ): 5.33 (br, 2H), 3.98-4.61 (br m, 5H),

Table 1. Molecular weight and composition of the linear and comb polymers used in this study.

Linear polymers			Comb polymers			
Polymers	DP_n[a]	M_n[a] (g/mol)	Polymers[b]	$M_{n,\,theo}$[c] (g/mol)	M_n[d] (g/mol)	Đ[d]
(*D*,*L*)K100	90-110	18800-23000	*L*K5	31000	33400	1.30
*L*K100	90-110	18800-23000	*L*K5SB-26	38600	42900	1.35
(*D*,*L*)E100	90-110	13600-16600	*L*K5SB-44	50500	44500	1.45
*L*E100	90-110	13600-16600	*L*K5SB-65	68500	43900	1.52
			*L*K5SB-88	126000	125700	1.77
			*L*E5	54500	35200[e]	

[a]Number-average degree of polymerization (DP_n) and M_n determined using NMR spectroscopy, as provided by the manufacturer. [b]Copolymers of *L*K5-COE and SB-COE are named *L*K5SB-X, where X indicates mol% SB units compared to the total polymer composition (*L*K5 + SB units), as determined by ^{1}H NMR spectroscopy. [c]$M_{n,theo}$ = ([monomer]:[initiator])*conversion*(molecular weight per repeat unit), assuming 100% conversion for *L*KSB-88. [d] Estimated relative to linear PMMA standards by SEC eluting in TFE. [e]M_w determined by SEC-MALS eluting in aqueous solution containing 5% ammonium phosphate and 3% acetonitrile (dn/dc of *L*E5 = 0.1058).

2.61-3.16 (br m, 10H), 2.31 (br, 1H), 0.56-2.17 (br m, 40H). SEC (0.02 M NaTFAc TFE, PMMA standards): M_n = 33400 g/mol, Đ = 1.30.

Poly(E5-COE), LE5. Monomer solution: *L*E5-COE (0.2 g, 0.185 mmol) in TFE (0.26 mL) and DCM (0.99 mL); catalyst solution (0.002 g, 0.003 mmol, 0.05 mL). Mass recovery = 93%. Deprotection: precipitate (0.19 g) was dissolved in a TFA/H_2O/TIPS solution (95/2.5/2.5 % v/v, ~8 mL). Product was dissolved in NaCl solution (2 M, ~2 mL), dialyzed against NaCl (2M, 1 L) then water, and re-lyophilized to afford a white powder in 58% yield (81 mg). ^{1}H NMR (500 MHz, D_2O, δ): 5.41 (br, 2H), 4.34 (br, 5H), 0.93-2.78 (br m, 31H). SEC-MALS (aqueous solution containing 5% ammonium phosphate and 3% acetonitrile): dn/dc = 0.1058, M_w = 47700 g/mol.

2.5. Preparation of Stock Solutions

Linear polymer stock solutions were prepared at 10 mM and comb polymer stock solutions were prepared at 1 mM concentrations in Millipore water, and adjusted to pH 7.00±0.05 using 1 M hydrochloric $acid_{(aq)}$ and/or 1 M sodium $hydroxide_{(aq)}$ and a Mettler Toledo Inlab pH probe attached to a Fisher Scientific Accuet pH meter. Sodium chloride stock solutions were prepared similarly at 2 $M_{(aq)}$.

2.6. Preparation of Complex Coacervates

Samples were prepared either by hand or using a Beckman Coulter Biomek NX_p pipetting robot equipped with a Span-8 pod, an orbital shaker, and a gripper. Complexation was performed using stoichiometric quantities of oppositely charged polypeptides at a total polymer concentration of 1 mM at pH 7.0, where it is appropriate to assume all polymers are fully charged. Milli-Q water and NaCl, if applicable, were mixed in a microcentrifuge tube (1.5 mL, Eppendorf) by hand, or in a 96-well plate by the Biomek pipetting robot, followed by addition of the polyanion and vigorous vortexing. The polycation was then added to reach a final volume of 120 µL, if prepared by hand, or 150 µL, if prepared by the Biomek pipetting robot. The order of addition did not have a significant effect on complex formation (Figure S6). The final mixture was vortexed vigorously and distributed into a 384-well plate as three 32-µL aliquots. All samples were prepared in triplicate except for the comb-comb systems where material limitations resulted in a single trial.

2.7. Turbidimetry and Optical Microscopy

Turbidity experiments were performed on each aliquot in triplicate using a Biotek, Inc. Synergy H1 UV spectrophotometer. A wavelength of 562 nm was used to measure turbidity, as the polymers do not absorb light at this wavelength. Measurements were performed in triplicate, and the data were plotted as the average of triplicate samples, with error bars indicating the standard deviation. Critical salt concentrations were estimated from turbidity readings and confirmed by visual inspection using a Fisher Scientific Evos XL Core optical microscope.

3. Simulation Methods

Comb polymers were simulated using a restricted primitive model (RPM) representation,[66] where charged residues were represented as hard spheres of radius a that interact via Coulomb potentials in a continuum solvent with relative dielectric constant $\epsilon_r = 78.5$. Polyelectrolytes and charged comb branches were treated as connected spheres of unit charge. This model cannot resolve atomistic detail, therefore some effects (*i.e.*, hydrophobic interactions, Hofmeister effects) were neglected.[67] Nevertheless, this model captures correlated electrostatics crucial to modelling coacervation.[68-70]

3.1. Monte Carlo (MC) Simulations of Linear and Comb Polymers

MC simulations were performed on combinations of linear and/or comb polyelectrolytes. Linear species consist of $N\times n_i$ charged monomers, where N is the degree of polymerization, and n_i is the number of polycations ($i = P+$) or polyanions ($i = P-$). Comb species consist of $3\times N_C\times n_i$ backbone monomers, where N_C is the degree of polymerization. The factor of 3 arises from the three polymer backbone beads per monomer unit, as shown in the schematic in Figure 4. Every three backbone beads, there is a branch of length n_B positively charged beads, leading to $n_B\times N_C\times n_i$ charged beads in the system. In addition to the polymer beads, there are n_+ cation and n_- anion beads accounting for both counterions and added salt. Each charged polyelectrolyte and salt bead has a radius a, while uncharged backbone beads are not simulated with excluded volume. The latter model attribute is chosen as a fit parameter to match simulation and experimental results, and reflects (1) the lack a strongly bound hydration shell around the uncharged backbone, in contrast with the hydration shell around the charged species, and (2) a slight 'effective' hydrophobicity.

This model is simulated in an NVT ensemble, and all species are at positions $\boldsymbol{r}_i^{\alpha}$, where i is the index identifying a specific ion or monomer and α specifies the type of bead (P+,P–,+,–, or 0 for polycation, polyanion, cation, anion, and backbone beads, respectively). All particles contribute to the system energy U given by:

$$U = U_{HS} + U_E + U_B + U_\theta$$

U_{HS} is the hard sphere contribution that prevents bead overlap:

$$U_{HS} = \sum_{\alpha,\beta}\sum_{i,j} u_{HS}(r_{ij}^{\alpha\beta})$$

This summates the pairwise contributions to the potential u_{HS} that is a function of the distance $r_{ij}^{\alpha\beta} = |\boldsymbol{r}_i^{\alpha} - \boldsymbol{r}_j^{\beta}|$ between beads i and j on species α and β:

$$u_{HS}\left(r_{ij}^{\alpha\beta}\right) = \begin{cases} \infty & r_{ij}^{\alpha\beta} < \sigma_{ij} \\ 0 & r_{ij}^{\alpha\beta} \sigma_{ij} \end{cases}$$

Here, σ_{ij} is the minimum possible distance between i and j, which is only nonzero when both species are charged ($\sigma_{ij} = 2a$). U_E is the Coulomb potential:

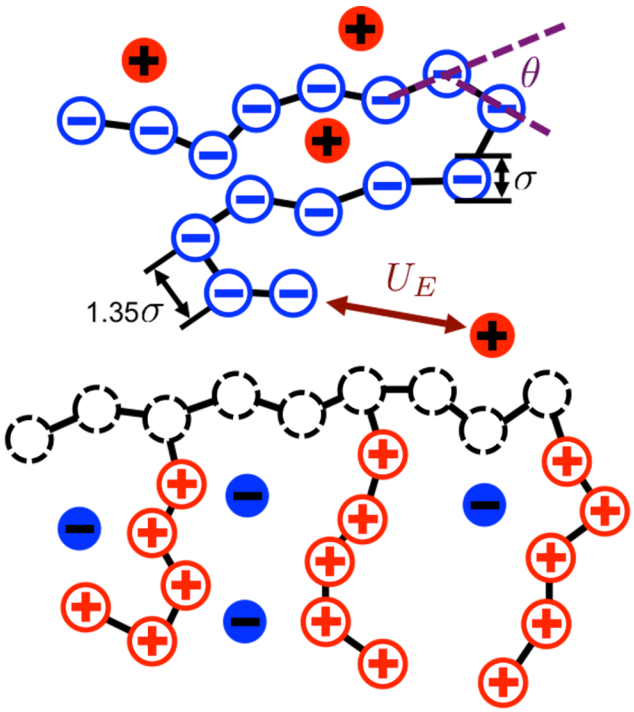

Figure 4. Schematic demonstrating the molecular model used for linear and comb polymers in MC simulations. Linear chains (polyanion shown) are connected chains of negative charges with diameter σ. The chains are semiflexible, due to a bending potential that imposes an energetic penalty on the bond angle θ. There are electrostatic interactions between all charged species, including polyelectrolytes and salt ions. Comb polymers have branches that consist of five charges to represent pentalysine branches. Backbone chain beads are uncharged, and do not have any excluded volume.

$$U_E = \sum_{\alpha,\beta}\sum_{i,j}\frac{q_\alpha q_\beta}{4\pi\epsilon_0\epsilon_r r_{ij}^{\alpha\beta}}$$

q_α is the per-bead charge of species α and ϵ_0 is the vacuum permittivity. We use standard Ewald summation to calculate electrostatic interactions in the simulation.[71] U_B is the bonding potential:

$$U_B = \sum_{\alpha=P+,P-,0}\sum_{i^*} u_B(r_{i,i-1}^{\alpha,\alpha})$$

This is only included for polymeric species, and the asterisk on the summation i^* denotes that we only consider connected beads (as shown in Figure 4). The pair potential is given by:

$$u_B(r_{i,i-1}^{\alpha,\alpha}) = \begin{cases} 0 & 2.7a \le r_{i,i-1}^{\alpha,\alpha} < 2.9a \\ \infty & otherwise \end{cases}$$

Finally, we include an angle potential U_θ:

$$U_\theta = \sum_{\alpha=P+,P-,0}\sum_{i^*} u_\theta(\boldsymbol{r}_{i-1}^{\alpha},\boldsymbol{r}_i^{\alpha},\boldsymbol{r}_{i+1}^{\alpha})$$

Once again, the asterisk indicates that the sum is only over bonded species. The pair potential u_θ is:

$$u_\theta(\boldsymbol{r}_{i-1}^{\alpha},\boldsymbol{r}_i^{\alpha},\boldsymbol{r}_{i+1}^{\alpha}) = \frac{\kappa_\theta}{2}\theta_i^2$$

κ_θ is the bending constant and θ_i is the angle formed by bonds on either side of bead index i. We parameterize our model with values $a = 0.212\,\text{nm}$ and $\kappa_\theta = 3.3k_BT$. Simulations include 4 chains of each species, each with 100 charged beads ($N = 120, N_C = N/n_B$), and are run for 1.5×10^7 cycles.

3.2. Monte Carlo-Informed Field Theory

Excess chemical potentials μ_{EXC}^{α} for all species α are calculated using standard Widom insertion methods,[71] modified to account for the charged and polymeric species. Electroneutrality is maintained by inserting positive and negative species jointly; for the polyelectrolyte species, this involves extending branches for combs or adding monomers to the end of a chain. This is a modified version of a method developed by Kumar, *et al.*[72] To incorporate the thermodynamic contributions of the various charges along the branches, we include a few partial branches that are 'grown' *via* Widom insertion.

The entire set of excess chemical potentials was tabulated at a number of values of ϕ_S and ϕ_P, and thermodynamic integration is used to calculate the excess free energy from a reference state ϕ_S^0 and ϕ_P^0:[73]

$$f_{EXC}(\phi_S,\phi_P) = \int_{\phi_S^0,\phi_P^0}^{\phi_S,\phi_P^0}\mu_{EXC}^{S}(\phi_S',\phi_P^0)d\phi_S' + \int_{\phi_S,\phi_P^0}^{\phi_S,\phi_P}\mu_{EXC}^{P}(\phi_S,\phi_P')d\phi_P'$$

This thus provides a simulation-informed excess free energy that can be incorporated into a Flory-Huggins-like expression for the free energy:

$$\frac{\mathcal{F}a^3}{Vk_BT} = \frac{\phi_P}{N_C}\ln\frac{\phi_P}{2} + \phi_S\ln\frac{\phi_S}{2} + \phi_W\ln\phi_W + f_{EXC}(\phi_P,\phi_S)$$

This free energy expression is used to numerically calculate the binodal. It has been shown that this matches computationally demanding techniques such as Gibbs Ensemble Monte Carlo.[73]

4. Results

We sought to understand the effect of branching on complex coacervation. While it is straightforward to imagine how oppositely charged linear polymers interact to form a charge-neutral coacervate complex, it is unclear the extent to which a mismatch in polymer architecture, due to branching, might alter this interaction. Here, we utilized oligopeptide-grafted poly(cyclooctene)s as a model system. We synthesized penta(*L*-lysine) (*L*K5) and penta(*L*-glutamate) (*L*E5) comb polymers by solid phase peptide synthesis and ring-opening metathesis polymerization (ROMP), using similar methods as those described in previous reports[64,65] (Figure 2). We then compared the self-assembly and stability of complex coacervates resulting from complexation between oppositely charged linear polymers, a linear and a comb polymer, and two comb polymers using turbidity measurements, optical microscopy, and Monte Carlo simulations. Additionally, we

investigated the effect of incorporating pendant sulfobetaine (SB) moieties along the length of the polymer (Figure 3), while maintaining a constant number of charged groups.

4.1. Effect of Polymer Architecture on the Stoichiometry of Complex Coacervation

Turbidimetry was used to examine the effect of polymer architecture (*i.e.*, linear *vs*. comb) on the formation and stability of complex coacervates. All experiments were performed at pH 7.0. Under these conditions, it is reasonable to assume that cationic poly(lysine) and anionic poly(glutamate) are both fully charged.[37,41] For linear polymers, a maximum in the turbidity signal would be expected to occur at net neutral conditions, with the number of positive charges equalling the number of negative charges.[37] However, it was unclear whether steric considerations associated with the comb architecture might frustrate this interaction.

Figure 5a compares the turbidimetry results for linear poly(*L*-lysine) and a pentalysine comb polymer (*L*K5) in complexes with linear poly(*D,L*-glutamate) as a function of the mole fraction of the cationic monomer. Figure 5b plots the same data on a charge basis. Linear polymers contain one charge per monomer unit, while the pentalysine comb polymers contain four charges per monomer unit from the five lysines and one carboxylate (Figure 2a). As expected for the system of linear polymers, we observed a maximum in the turbidity signal at approximately net-neutral conditions, or a cationic monomer mole fraction of ~0.5 (Figure 5a,b). However, for the comb-linear system we observed a peak in the turbidity data at a cationic mole fraction of ~0.2, or a ratio of one pentalysine monomer for every four glutamate monomers (Figure 5a). While not as directly intuitive, this result correlates with the +4 net charge of a pentalysine branch. Replotting of these data on a charge basis (Figure 5b) shows alignment of the turbidity signals between the linear and comb experiments, and demonstrates that the cyclooctene comb architecture does not sterically frustrate electrostatic interactions with linear poly(*D,L*-glutamate). All subsequent experiments were performed using the charge-neutral stoichiometries shown in Figures 5a,b.

4.2. Effect of Polymer Architecture on Coacervate Phase Behaviour

Complex coacervate phase behaviour is typically described as a function of polymer and salt concentration (Figure 5d).[2,4,12,68,70,74-76] Binodal curves can be specified for a given stoichiometric composition, pH, and temperature. Complex coacervation is observed for samples prepared at a concentration falling within the two-phase region beneath the binodal curve, while no phase separation is observed at concentrations above the binodal. Preparation of a sample within the two-phase region will result in the formation of a polymer-rich coacervate phase and a polymer-poor supernatant phase, the equilibrium concentrations of which are defined by a tie-line (Figure 5d).

Turbidity experiments identify the location of the binodal curve by varying salt concentration for a given polymer concentration. Typical salt curves, which plot turbidity as a function of salt concentration, show a sharp increase in turbidity with the addition of small amounts of salt for coacervate-forming systems.[1,37,41] This signal decreases with further increases in the total salt concentration until a 'critical salt concentration' is reached, above which phase separation is no longer observed. This critical salt concentration provides a means for comparing the stability of different coacervate samples, and scales with the size of the two-phase region. Figure 5c shows the salt curves for linear poly(*L*-lysine) and a pentalysine comb polymer in complex with linear poly(*D,L*-glutamate), as well as the pentalysine comb polymer (*L*K5) in complex with the pentaglutamate comb polymers (*L*E5).

We observed a significantly lower critical salt concentration for the comb-linear coacervates (350 mM NaCl) than the linear-linear system (600 mM NaCl). However, the magnitude of the turbidity signal for the comb-linear system was significantly higher than for the all-linear version. While the higher turbidity signal for the linear-comb system would be anticipated due to the higher molecular weight of the pentalysine comb polymer *L*K5 (~30 kDa) compared to the linear polylysine (~20 kDa, Table 1), the lower critical salt concentration of the linear-comb system was unexpected. The larger number of lysine groups per chain in the comb polymer (~150) relative to the linear polymers (90-110) would be expected to result in a higher critical salt concentration, based on previous experimental results[37] and mean-field theories such as Voorn-Overbeek.[4,12,74,76,77]

To address the difficulty of predicting the phase behaviour of non-linear molecular architectures, we performed molecular simulations of linear and comb polycations in complexation with linear polyanions, and used Monte Carlo-informed Flory Huggins theory to construct the binodal curves (Figure 5d). These simulations are capable of capturing the effect of chain architecture on the phase diagrams of coacervation, due to the incorporation of combs directly into the molecular model (Section 3.1 and Figure 4). Replacing one of these linear polyelectrolytes with a comb polyelectrolyte results in a significant change in the two-phase region. This is dependent on the length of the branches, with a few values of n_B shown. Short branches ($n_B = 3$) only undergo phase separation up to ~300 mM NaCl, while the phase behaviour of longer branches ($n_B = 8$) approaches that of linear-linear coacervates. These results are in agreement with previous experimental and simulation results that focused on the binding of DNA with the same polylysine comb polymers for applications in gene delivery, with the longest comb polymer approaching those for a linear polylysine.[83] Extrapolation from these data suggests near-quantitative agreement with the experimentally observed critical salt concentration in Figure 5c for combs of ($n_B = 4$), in the range of 300 mM to 500 mM.

We note that the Monte Carlo simulations include charge without resolving atomistic detail, and therefore the close match between phase diagrams determined from experiments and simulation suggests that the smaller binodal regions of

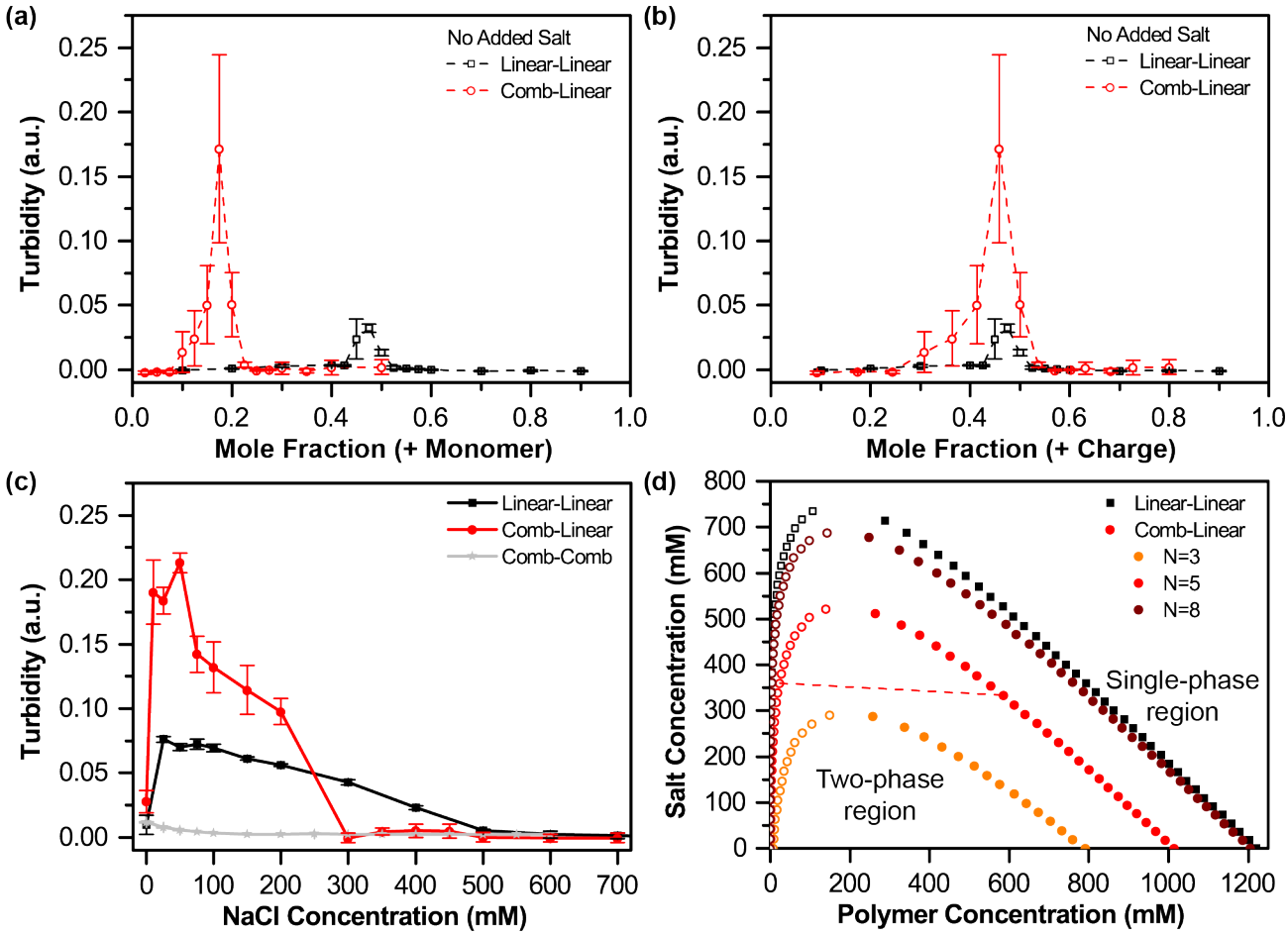

Figure 5. Plot of turbidity as a function of **(a)** mole fraction of the cationic monomer (*i.e.*, a single lysine for linear polymers, and a pentalysine branch for comb polymers) and **(b)** mole fraction of cationic charges (based on the total number of charged groups) in the absence of added salt. Data are shown comparing coacervation between two linear homopolypeptides, poly(*L*-lysine) (*L*K100) and poly(*D*,*L*-glutamate) ((*D*,*L*)E100, black squares), and the pentalysine comb polymer *L*K5 with a linear poly(*D*,*L*-glutamate) ((*D*,*L*)E100, red circles). (c) Plot of turbidity as a function of salt concentration comparing complex formation between the two linear polymers (black squares), the *L*K5 comb polymer and a linear poly(*D*,*L*-glutamate) ((*D*,*L*)E100, red circles), and two comb polymers (*L*K5 and *L*E5). All samples were prepared at 1 mM total monomer concentration and pH = 7.0. Complexes were prepared by adding the polycation to a solution containing a mixture of the polyanion and the desired quantity of salt. **(d)** Simulated binodal curves as a function of polymer and salt concentration for charge neutral complexes of the linear-linear (black squares) and comb-linear (circles) systems for different branch lengths $n_B = 3,5,8$. Complex coacervation occurs for samples prepared at conditions beneath the binodal phase boundary. A sample prepared at a concentration within the two-phase region will phase separate along (dashed) tie-lines to form a polymer-rich coacervate phase (closed symbols) and a polymer-poor supernatant phase (open symbols).

the comb polymer-containing coacervate systems result from changes in the thermodynamic driving force for coacervation, rather than from differences in polymer chemistry, such as the hydrophobicity of the backbone.

Coacervation is known to be entropically driven[39,78,79] as described by counterion condensation and release.[80] In counterion condensation, high charge-density polyelectrolytes recruit oppositely charged salt ions from solution to satisfy required charge neutrality and lower their effective charge density.[81,82] During coacervation, oppositely charged polymers can replace these condensed counterions, which regain their translational entropy. In linear polymers, the driving force for counterion condensation is strong because all charges along the chain feel the energetic penalty of the un-neutralized charges on the neighbouring monomer units. However, in combs where the linear sequence of charged groups is shorter, many of the charged groups have only one charged neighbour because they reside at the beginning or end of the branch. As such, the comb polymers are postulated to condense fewer counterions, leading to a weaker driving force for coacervation.

We also investigated complexation between two comb polymers, poly(penta-L-lysine) *L*K5 and poly(penta-L-glutamate) *L*E5. Analogous to the charge state of the pentalysine comb polymer (*i.e.*, +4 net charge per branch), the *L*E5 comb consists of five anionic glutamates and a cationic *C*-terminal amide. Surprisingly, no coacervation was observed in simulations, and only a very weak turbidity signal was observed at low salt concentrations (Figure 5c), which optical microscopy confirmed to be solid precipitation (Figure 6). While electrostatic complexes of oppositely charged homochiral peptides have been shown to result in the formation of solid precipitates due to the formation of interpeptide hydrogen bonding,[41] such effects were predicted to require a minimum peptide chain length of ~8 amino acids,[40,42] and were thus not anticipated for this comb-comb system.

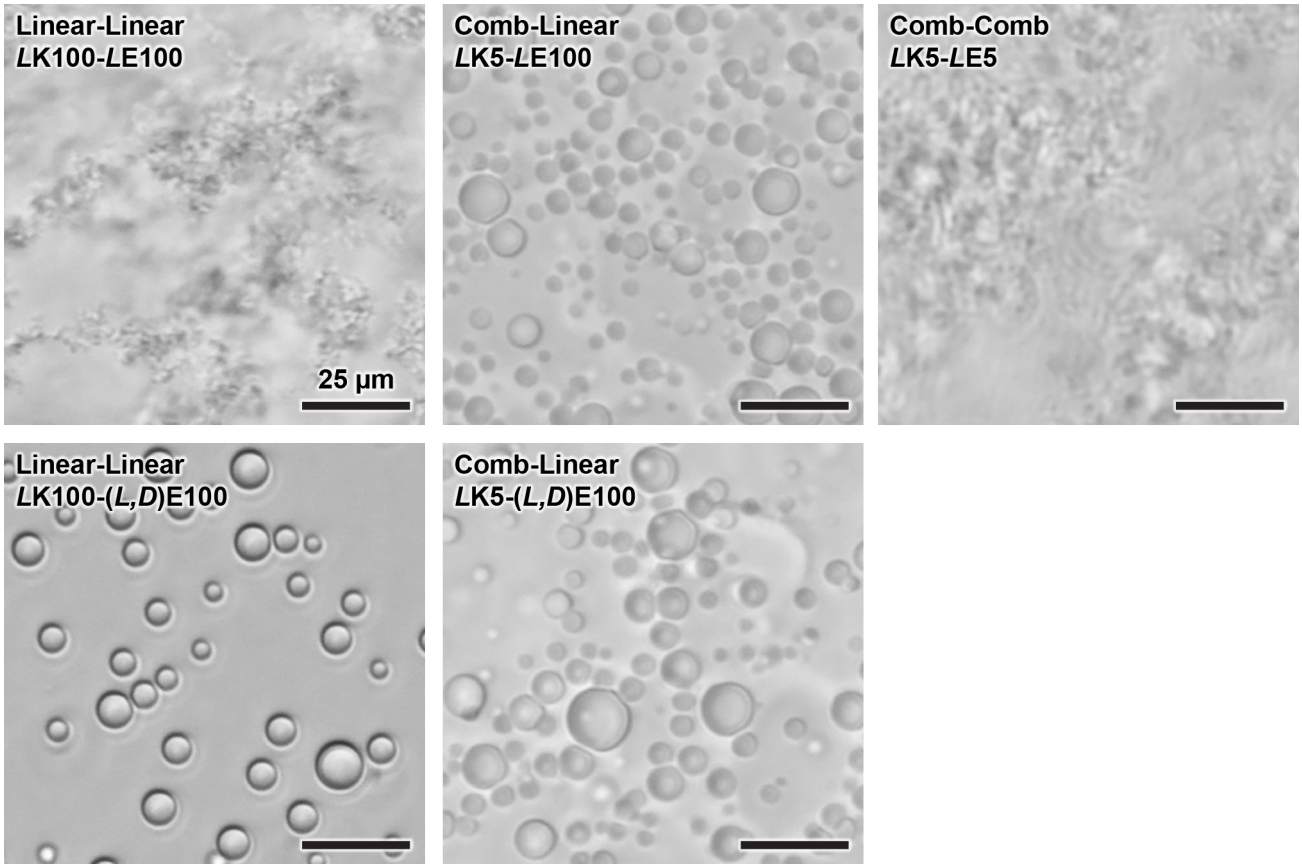

Figure 6. Bright-field optical micrographs showing polyelectrolyte complexes resulting from stoichiometric electrostatic complexation of linear and comb polypeptides. Precipitation was observed for complexes of homochiral, linear poly(*L*-lysine) (*L*K100) with poly(*L*-glutamate) (*L*E100) and for comb-comb complexes of homochiral penta(*L*-lysine) (*L*K5) and penta(*L*-glutamate) (*L*E5) polymers. In contrast, liquid coacervates formed from the complexation of homochiral, linear poly(*L*-lysine) (*L*K100) with racemic, linear poly(*D,L*-glutamate) ((*D,L*)E100), and the complexation between homochiral, penta(*L*-lysine) (*L*K5) with linear poly(*L*-glutamate) (*L*E100) and poly(*D,L*-glutamate) ((*D,L*)E100). All samples were prepared at 3-6 mM total monomer concentration and pH = 7.0. Complexes were prepared by adding the polycation to a solution containing a mixture of the polyanion and the desired quantity of salt.

4.3. Effect of Peptide Chirality and Comb Architecture on Complex Coacervation

The ability to form liquid complex coacervates using simple homopolypeptides depends critically on chirality-induced disruption of backbone hydrogen bonds.[41] Molecular dynamics simulations and experiments have indicated that sequences containing ~8 or fewer homochiral amino acids prevent the formation of stable runs of hydrogen bonds that would lead to a β-sheet structure and subsequent precipitation.[40,42] Consequently, we hypothesized that a comb polymer with branches of only 5 homochiral amino acids would be resistant to β-sheet formation and precipitation. Figure 6 compares optical micrographs of polyelectrolyte complexes as a function of chain architecture and peptide chirality. Consistent with previous reports,[41] we observed the formation of solid precipitates for complexes formed from linear poly(*L*-lysine) and poly(*L*-glutamate). Similarly, we observed the formation of liquid complex coacervates from homochiral poly(*L*-lysine) and racemic poly(*D,L*-glutamate). The formation of liquid coacervates for comb-linear architectures, however, proved insensitive to the chirality of the linear polypeptide, as seen for complexation of a *L*K5 comb polymer with both homochiral and racemic linear poly(glutamates). Liquid coacervates resulting from these comb-linear polymers was expected due to the short pentalysine branches on the comb polymers.[40,42] This represents a potentially powerful strategy for designing tailored, peptide-based coacervate materials for future applications.

We also investigated polyelectrolyte complexation between the cationic *L*K5 and anionic *L*E5 comb polymers. Based on our initial hypothesis and the results of our comb-linear experiments, we anticipated the formation of liquid coacervates for this comb-comb system, but instead observed only precipitation (Figure 6). We explain this discrepancy between hypothesis and experiment in the context of MC simulation results, which showed no evidence of phase separation, determined via direct comparison of the minimum free energy of a phase-separated system to the free energy of a homogeneous solution of oppositely charged polyelectrolytes. For all polymer and salt concentrations, the homogeneous solution for comb-comb systems had the lowest free energy, thus eliminating the driving force for coacervation.

While coacervation has been observed previously for sequence-controlled polypeptides containing repeating blocks

of charged amino acids,[50] the linear connectivity of such short charged blocks along the chain was sufficient to facilitate coacervation. In contrast, the comb architecture appears to disrupt the connectivity and cooperativity of this self-assembly process, while facilitating chain alignment to stabilize β-sheet formation. At first glance, the disparate behaviour of enhanced hydrogen bonding and decreased electrostatics are counterintuitive. However, since hydrogen bonding can be enhanced by chain alignment and the number of condensed counterions, the entropic driving force for complexation is an innate property of a given polymer geometry.

4.4. Effect of the Incorporation of Zwitterionic Moieties on Complex Coacervation

The comb polymer platform enabled an additional investigation of the effect of incorporating hydrophilic zwitterionic moieties (*i.e.*, net-neutral groups with positive and negative charges on the same monomer unit) without altering the overall charge of the polymer or the local charge density of a single pendant pentalysine comb (Figure 1b). We tested whether charge-dipole interactions between the polyelectrolytes and the zwitterionic groups would affect charge-driven complexation. We chose sulfobetaine zwitterions for their ease of incorporation into the comb polymers.[64] The sulfobetaine monomers were incorporated from 0 to 88 mol% into the polymers by ring-opening metathesis copolymerization of *L*K5-COE and SB-COE, holding the [*L*K5-COE]:[initiator] ratio constant at 50 and varying the SB-COE feed to maintain the number of lysines per polymer chain (Figure 3).

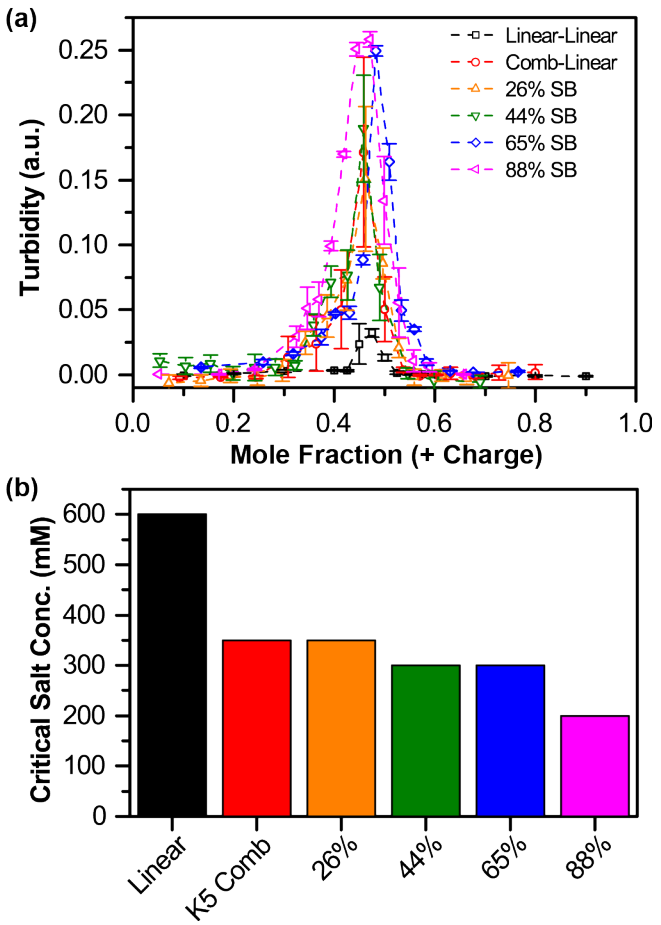

Figure 7. (a) Plot of turbidity as a function of the mole fraction of cationic charges present (based on the total number of charged groups) in the absence of added salt, comparing coacervation between two linear homopolypeptides, poly(*L*-lysine) with poly(*D,L*-glutamate) (*L*K100 and (*D,L*)E100, black squares) and comb-linear complexes formed from (*D,L*)E100 and pentalysine comb polymers with increasing sulfobetaine content (*L*K5SB-X, X = mol% SB). All samples were prepared at 1 mM total monomer concentration and pH = 7.0. Complexes were prepared by adding the specified polycation to a solution containing a mixture of linear poly(*D,L*-glutamate) (*D,L*)E100 and the desired quantity of salt. **(b)** Plot of critical salt concentration as a function of polymer architecture and sulfobetaine content.

Turbidimetry measurements shown in Figure 7a suggest that inclusion of zwitterions, even up to 88 mol%, did not significantly impact the charge stoichiometry of complex coacervation between a linear poly(glutamate) and the pentalysine-sulfobetaine comb polymers, *L*K5SB-X, where X = mol% SB compared to the total polymer composition (*L*K5 + SB units). However, across the samples studied, the number of lysines was maintained at a relatively constant level. Thus, even for polymers with the highest sulfobetaine loading (88%), the mass ratio of sulfobetaine to pentalysine units was nearly 2:1. It is possible for dipole effects to become significant if the polyelectrolyte content of the polymer was decreased, though such investigations are beyond the scope of this paper.

We also considered the impact of zwitterion content on coacervate phase behaviour. Using the critical salt concentration as a measure of stability, we observed that incorporation of 26% sulfobetaine did not significantly affect the phase behaviour (*i.e.,* critical salt concentration of 350 mM NaCl, Figure 7b). In fact, increasing the zwitterion content to 88% sulfobetaine, while maintaining similar numbers of lysines, resulted in only a ~42% decrease in the critical salt concentration to 200 mM NaCl. These results highlight the potential for formulating complex coacervates with enhanced biocompatibility and antifouling character due to the presence of zwitterions, while minimizing the fraction of charged groups required to achieve coacervate stability. Further examination of the effect of zwitterion chemistry and analogous strategies for incorporating hydrophilic groups on both linear and comb polymers will better elucidate specific design rules that balance the roles of charge-driven assembly with polymer architecture and composition.

5. Conclusions

In summary, we report the impact of polymer architecture on complex coacervation. By rearranging long, linear charge segments into comb-like polymer structures, both experimental and simulation results demonstrated a significant decrease in the overall stability of the coacervate materials formed from a comb polycation with a linear polyanion relative to those formed from equivalent linear polymers. Interestingly, no coacervate formation was observed from mixtures of comb polycations and comb polyanions. More specifically, for the peptide-based materials utilized, polymer architecture modulated the formation of hydrogen

bond-driven β-sheet structures that would be expected for homochiral linear polypeptides.[40-42] Subsequent incorporation of zwitterionic sulfobetaine pendant groups, while maintaining constant cation/anion stoichiometry, suggested the potential for the inclusion of comonomers, even at high loadings, without preventing coacervation.

This study provides insights into the ways in which polymer architecture and chemistry modulate self-assembly and complex coacervation. While we focused on the effects of branching and comb-type architectures, the use of a well-defined model system allowed for easy interpretation of the results and the potential for extension to additional architectures and chemistries. For example, polypeptide-based comb polymers have been demonstrated previously in the context of gene therapy to facilitate the successful complexation and enhanced release of genetic cargo.[48,83] However, many open questions remain, including the effect of branching density, minimum charge content requirements, and the impact of specific chemistries. Ultimately, the extensive tunability of coacervate-based materials should allow for tailoring of material properties in drug delivery, remediation, and catalysis, and will provide insight into the behaviour of analogous biological systems.

Acknowledgements

We thank Matthew Skinner for assistance with polymer synthesis and Yalin Liu for help with polymer characterization. B.M.J. acknowledges support from the University of Massachusetts, Amherst Commonwealth Honors College Fellowship, C.E.S. acknowledges support from NSF CAREER Award DMR-1654158 and use of the Extreme Science and Engineering Discovery Environment (XSEDE), which is supported by National Science Foundation Grant ACI-1053575. R.A.L. and T.E. acknowledge financial support from the National Science Foundation (NSF CBET 1403742) and facilities support from the Materials Research Science and Engineering Center (MRSEC DMR-0820506) on Polymers at the University of Massachusetts.

References

1 S. Perry, Y. Li, D. Priftis, L. Leon and M. Tirrell, *Polymers*, 2014, **6**, 1756–1772.
2 J. van der Gucht, E. Spruijt, M. Lemmers and M. A. C. Stuart, *J. Colloid Interface Sci.*, 2011, **361**, 407–422.
3 Y. Liu, H. H. Winter and S. L. Perry, *Adv. Colloid Interface Sci.*, 2017, **239**, 46–60.
4 C. E. Sing, *Adv. Colloid Interface Sci.*, 2017, **239**, 2–16.
5 C. G. de Kruif, F. Weinbreck and R. de Vries, *Curr. Opin. Colloid Interface Sci.*, 2004, **9**, 340–349.
6 A. Seweryn, T. Wasilewski and T. Bujak, *Ind. Eng. Chem. Res.*, 2016, **55**, 1134–1141.
7 S. L. Turgeon, C. Schmitt and C. Sanchez, *Curr. Opin. Colloid Interface Sci.*, 2007, **12**, 166–178.
8 F. Weinbreck, R. de Vries, P. Schrooyen and C. G. de Kruif, *Biomacromolecules*, 2003, **4**, 293–303.
9 T. H. Kalantar, C. J. Tucker, A. S. Zalusky, T. A. Boomgaard, B. E. Wilson, M. Ladika, S. L. Jordan, W. K. Li and X. Zhang, *J. Cosmet. Sci.*, 2007, **58**, 375–383
10 C. Schmitt and S. L. Turgeon, *Adv. Colloid Interface Sci.*, 2011, **167**, 63–70.
11 B.-C. Wu, B. Degner and D. J. McClements, *J. Phys.: Condens. Matter*, 2014, **26**, 464104.
12 W. C. Blocher and S. L. Perry, *WIREs Nanomed. Nanobiotechnol.*, 2017, **6**.
13 R. J. Stewart, C. S. Wang and H. Shao, *Adv. Colloid Interface Sci.*, 2011, **167**, 85–93.
14 N. R. Johnson and Y. Wang, *Expert Opin. Drug Delivery*, 2014, **11**, 1829–1832.
15 W. C. W. Chen, B. G. Lee, D. W. Park, K. Kim, H. Chu, K. Kim, J. Huard and Y. Wang, *Biomaterials*, 2015, **72**, 138–151.
16 A. Nolles, A. H. Westphal, J. A. de Hoop, R. G. Fokkink, J. M. Kleijn, W. J. H. van Berkel and J. W. Borst, *Biomacromolecules*, 2015, **16**, 1542–1549.
17 A. C. Obermeyer, C. E. Mills, X.-H. Dong, R. J. Flores and B. D. Olsen, *Soft Matter*, 2016, **12**, 3570–3581.
18 N. Pippa, R. Kalinova, I. Dimitrov, S. Pispas and C. Demetzos, *J. Phys. Chem. B*, 2015, **119**, 6813–6819.
19 A. Chremos and J. F. Douglas, *Soft Matter*, 2016, **12**, 2932–2941.
20 H. G. Bungenberg de Jong and H. R. Kruyt, *Kolloid-Z.*, 1930, **50**, 39–48.
21 R. Chollakup, J. B. Beck, K. Dirnberger, M. Tirrell and C. D. Eisenbach, *Macromolecules*, 2013, **46**, 2376–2390.
22 S. Ishii, J. Kaneko and Y. Nagasaki, *Biomaterials*, 2016, **84**, 210–218.
23 S. Lindhoud, R. de Vries, R. Schweins, M. A. Cohen Stuart and W. Norde, *Soft Matter*, 2009, **5**, 242–250.
24 S. Lindhoud and M. M. A. E. Claessens, *Soft Matter*, 2015, **12**, 408–413.
25 C. L. Cooper, P. L. Dubin, A. B. Kayitmazer and S. Turksen, *Curr. Opin. Colloid Interface Sci.*, 2005, **10**, 52–78.
26 C. Schmitt and S. L. Turgeon, *Adv. Colloid Interface Sci.*, 2011, **167**, 63–70.
27 C. Schmitt, C. Sanchez, S. Desobry-Banon and J. Hardy, *Crit. Rev. Food Sci. Nutr.*, 1998, **38**, 689–753.
28 G. Davidov-Pardo, I. J. Joye and D. J. McClements, *Food-Grade Protein-Based Nanoparticles and Microparticles for Bioactive Delivery: Fabrication, Characterization, and Utilization*, Elsevier Inc., 1st edn. 2015, vol. 98.
29 D. Priftis, K. Megley, N. Laugel and M. Tirrell, *J. Colloid Interface Sci.*, 2013, **398**, 39–50.
30 M. Zhao and N. S. Zacharia, *Macromol. Rapid Commun.*, 2016, **37**, 1249–1255.
31 D. Priftis, X. Xia, K. O. Margossian, S. L. Perry, L. Leon, J. Qin, J. J. de Pablo and M. Tirrell, *Macromolecules*, 2014, **47**, 3076–3085.
32 J. Warnant, N. Marcotte, J. Reboul, G. Layrac, A. Aqil, C. Jerôme, D. A. Lerner and C. Gérardin, *Anal. Bioanal. Chem.*, 2012, **403**, 1395–1404.
33 A. B. Kayitmazer, H. B. Bohidar, K. W. Mattison, A. Bose, J. Sarkar, A. Hashidzume, P. S. Russo, W. Jaeger and P. L. Dubin, *Soft Matter*, 2007, **3**, 1064–1076.
34 A. Prokop, D. Hunkeler, S. DiMari, M. A. Haralson and T. G. Wang, *Adv. Polym. Sci.*, 1998, **136**, 1–51.
35 H. Chu, N. R. Johnson, N. S. Mason and Y. Wang, *J. Controlled Release*, 2011, **150**, 157–163.
36 D. Priftis, R. Farina and M. Tirrell, *Langmuir*, 2012, **28**, 8721–8729.

37 D. Priftis and M. Tirrell, *Soft Matter*, 2012, **8**, 9396–9405.
38 D. Priftis, L. Leon, Z. Song, S. L. Perry, K. O. Margossian, A. Tropnikova, J. Cheng and M. Tirrell, *Angew. Chem. Int. Ed.*, 2015, **127**, 11280–11284.
39 D. Priftis, N. Laugel and M. Tirrell, *Langmuir*, 2012, **28**, 15947–15957.
40 K. Q. Hoffmann, S. L. Perry, L. Leon, D. Priftis, M. Tirrell and J. J. de Pablo, *Soft Matter*, 2015, **11**, 1525–1538.
41 S. L. Perry, L. Leon, K. Q. Hoffmann, M. J. Kade, D. Priftis, K. A. Black, D. Wong, R. A. Klein, C. F. Pierce, K. O. Margossian, J. K. Whitmer, J. Qin, J. J. de Pablo and M. Tirrell, *Nat. Commun.*, 2015, **6**, 6052.
42 N. M. Pacalin, L. Leon and M. Tirrell, *Eur. Phys. J. Spec. Top.*, 2016, **225**, 1805–1815.
43 K. Kataoka, H. Togawa, A. Harada, K. Yasugi, T. Matsumoto and S. Katayose, *Macromolecules*, 1996, **29**, 8556–8557.
44 A. Harada and K. Kataoka, *Science*, 1999, **283**, 65–67.
45 A. Harada and K. Kataoka, *Macromolecules*, 1995, **28**, 5294–5299.
46 A. Koide, A. Kishimura, K. Osada, W.-D. Jang, Y. Yamasaki and K. Kataoka, *J. Am. Chem. Soc.*, 2006, **128**, 5988–5989.
47 A. Wibowo, K. Osada, H. Matsuda, Y. Anraku, H. Hirose, A. Kishimura and K. Kataoka, *Macromolecules*, 2014, **47**, 3086–3092.
48 S. S. Parelkar, D. Chan-Seng and T. Emrick, *Biomaterials*, 2011, **32**, 2432–2444.
49 M. Amblard, J. A. Fehrentz, J. Martinez and G. Subra, *Mol. Biotechnol.*, 2006, **33**, 239–254.
50 L. W. Chang, T. K. Lytle, M. Radhakrishna, J. J. Madinya, J. Velez, C. E. Sing and S. L. Perry, *Submitted*.
51 D. Y. Ko, M. Patel, B. K. Jung, J. H. Park and B. Jeong, *Biomacromolecules*, 2015, **16**, 3853–3862.
52 J. B. Schlenoff, *Langmuir*, 2014, **30**, 9625–9636.
53 C.-C. Chang, R. Letteri, R. C. Hayward and T. Emrick, *Macromolecules*, 2015, **48**, 7843–7850.
54 G. Hu and T. Emrick, *J. Am. Chem. Soc.*, 2016, **138**, 1828–1831.
55 S. Chen, L. Li, C. Zhao and J. Zheng, *Polymer*, 2010, **51**, 5283–5293.
56 L. Zhang, Z. Cao, T. Bai, L. Carr, J.-R. Ella-Menye, C. Irvin, B. D. Ratner and S. Jiang, *Nat. Biotechnol.*, 2013, **31**, 553–556.
57 A. B. Lowe and C. L. McCormick, *Chem. Rev.*, 2002, **102**, 4177–4190.
58 J. B. Schlenoff, *Langmuir*, 2014, **30**, 9625–9636.
59 Z. G. Estephan, P. S. Schlenoff and J. B. Schlenoff, *Langmuir*, 2011, **27**, 6794–6800.
60 M. A. Hillmyer, W. R. Laredo and R. H. Grubbs, *Macromolecules*, 1995, **28**, 6311–6316.
61 D. Hartley, *J. Am. Chem. Soc.*, 1962, 4722–4723.
62 E. C. Ashby and D. Coleman, *J. Org. Chem.*, 1987, **52**, 4554–4565.
63 J. A. Love, J. P. Morgan, T. M. Trnka and R. H. Grubbs, *Angew. Chem. Int. Ed.*, 2002, **41**, 4035–4037.
64 A. F. Ghobadi, R. Letteri, S. S. Parelkar, Y. Zhao, D. Chan-Seng, T. Emrick and A. Jayaraman, *Biomacromolecules*, 2016, **17**, 546–557.
65 R. B. Breitenkamp, Z. Ou, K. Breitenkamp, M. Muthukumar and T. Emrick, *Macromolecules*, 2007, **40**, 7617–7624.
66 J. P. Hansen and I. R. McDonald, *Theory of Simple Liquids*, Elsevier, Boston, 3rd edn. 2006.
67 A. Salis and B. W. Ninham, *Chem. Soc. Rev.*, 2014, **43**, 7358–7377.
68 M. Radhakrishna, K. Basu, Y. Liu, R. Shamsi, S. L. Perry and C. E. Sing, *Macromolecules*, 2017, **50**, 3030–3037.
69 M. Radhakrishna and C. E. Sing, *Macromol. Chem. Phys.*, 2015, **217**, 126–136.
70 S. L. Perry and C. E. Sing, *Macromolecules*, 2015, **48**, 5040–5053.
71 D. Frenkel and B. Smit, *Understanding Molecular Simulation*, Elsevier, 2nd edn. 2002.
72 S. K. Kumar, I. Szleifer and A. Z. Panagiotopoulos, *Phys. Rev. Lett.*, 1991, **66**, 2935–2938.
73 T. K. Lytle, M. Radhakrishna and C. E. Sing, *Macromolecules*, 2016, **49**, 9693–9705.
74 J. Qin, D. Priftis, R. Farina, S. L. Perry, L. Leon, J. Whitmer, K. Hoffmann, M. Tirrell and J. J. de Pablo, *ACS Macro Lett.*, 2014, **3**, 565–568.
75 J. Qin and J. J. de Pablo, *Macromolecules*, 2016, **49**, 8789–8800.
76 E. Spruijt, A. H. Westphal, J. W. Borst, M. A. Cohen Stuart and J. van der Gucht, *Macromolecules*, 2010, **43**, 6476–6484.
77 J. T. G. Overbeek and M. J. Voorn, *J. Cell. Comp. Physiol.*, 1957, **49**, 7–26.
78 Q. Wang and J. B. Schlenoff, *Macromolecules*, 2014, **47**, 3108–3116.
79 J. Fu and J. B. Schlenoff, *J. Am. Chem. Soc.*, 2016, **138**, 980–990.
80 A. Salehi and R. G. Larson, *Macromolecules*, 2016, **49**, 9706–9719.
81 G. S. Manning, *J. Chem. Phys.*, 1969, **51**, 924–933.
82 Z. Ou and M. Muthukumar, *J. Chem. Phys.*, 2006, **124**, 154902–1–154902–11.
83 R. M. Elder, T. Emrick and A. Jayaraman, *Biomacromolecules*, 2011, **12**, 3870–3879.